Supplementary Information

Efficient thermal management of electronic devices by constructing interlayer phonon bridges

Gaojie Han[1†], Hongli Cheng[1†], Yuezhan Feng[1*], Shiliang Zhang[2, 3], Jingwen Dong[1], Bing Zhou[1], Xianhu Liu[1*], Chuntai Liu[1*], Guangming Tao[2,3,4*], Changyu Shen[1]

[1] State Key Laboratory of Structural Analysis, Optimization and CAE Software for Industrial Equipment, National Engineering Research Center for Advanced Polymer Processing Technology, Zhengzhou University, Zhengzhou 450002, China

[2] Research Center for Intelligent Fiber Devices and Equipment, State Key Laboratory of New Textile Materials and Advanced Processing, School of Materials Science and Engineering and School of Physical Education, Huazhong University of Science and Technology, Wuhan 430074, China

[3] Department of Geriatrics and Key Laboratory of Vascular Aging, Ministry of Education, Tongji Hospital of Tongji Medical College, Huazhong University of Science and Technology, Wuhan 430030, China

[4] Center for Intelligent Health Interdisciplinary Science, Central China Normal University, Wuhan 430079, China

[†]These authors contributed to this work equally.

[*]Corresponding authors. E-mail: yzfeng@zzu.edu.cn (Y. Feng), xianhu.liu@zzu.edu.cn (X. Liu), ctliu@zzu.edu.cn (C. Liu), tao@hust.edu.cn (G. Tao)

Supplementary note 1.

Measurement for Specific heat capacity C_p

Specific heat capacity C_p was evaluated by using differential scanning calorimeter (DSC Q2000, TA Instruments) measurements. The widely accepted DSC sapphire method (ISO 11357-4), which uses sapphire as the standard sample, can significantly improve the accuracy of C_p measurements obtained by DSC. The C_p of ANF/BNNS film can be calculated by:

$$C_p = \frac{dH}{dT}\frac{1}{m} \tag{S1}$$

where dH is the heat required when the sample's temperature increases by dT, m is the weight of the film. By differentiating the numerator and denominator with respect to time, the rate of change of enthalpy dH/dt equals the DSC heat flow Φ, while the rate of change of sample temperature dT/dt corresponds to the heating rate β.

$$C_p = \frac{dH/dt}{dT/dt}\frac{1}{m} = \frac{\Phi}{\beta}\frac{1}{m} \tag{S2}$$

Under the same conditions, measurements were performed with sapphire as the standard sample.

$$C_{p\ Sapphire} = \frac{\Phi_{Sapphire}}{\beta}\frac{1}{m_{Sapphire}} \tag{S3}$$

$$C_{p\ Sample} = \frac{\Phi_{Sample}}{\beta}\frac{1}{m_{Sample}} \tag{S4}$$

and the C_p of the film was calculated based on the known C_p of sapphire.

$$C_{p\ Sample} = \frac{m_{Sapphire}}{m_{Sample}}\frac{(\Phi_{Sample}-\Phi_{blank\ run})}{(\Phi_{Sapphire}-\Phi_{blank\ run})}C_{p\ Sapphire} \tag{S5}$$

where $\Phi_{blank\ run}$ is DSC heat flow of empty crucible.

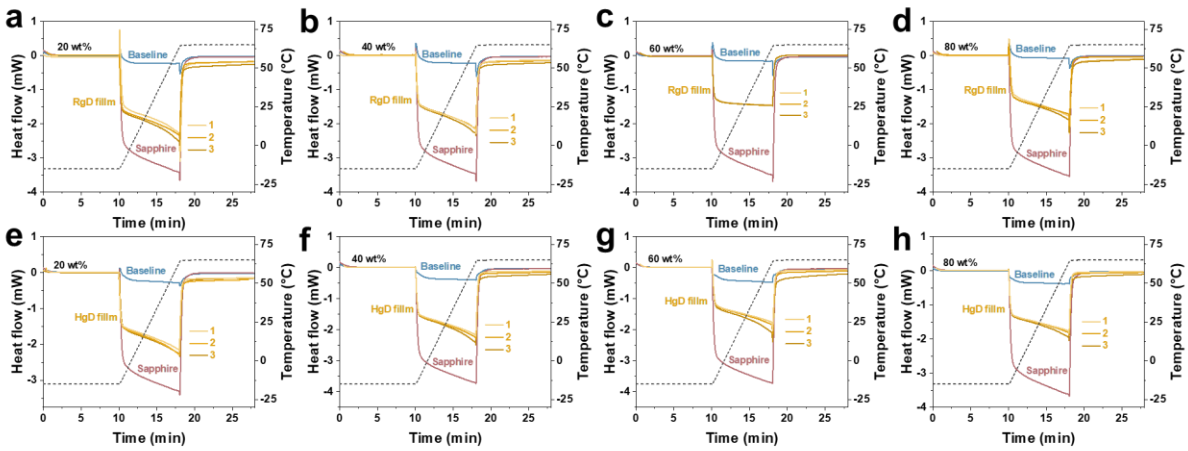

Supplementary Fig. 1. DSC curves for specific heat capacity calculations: (a-d) RgD ANF/BNNS films and (e-f) HgD ANF/BNNS films.

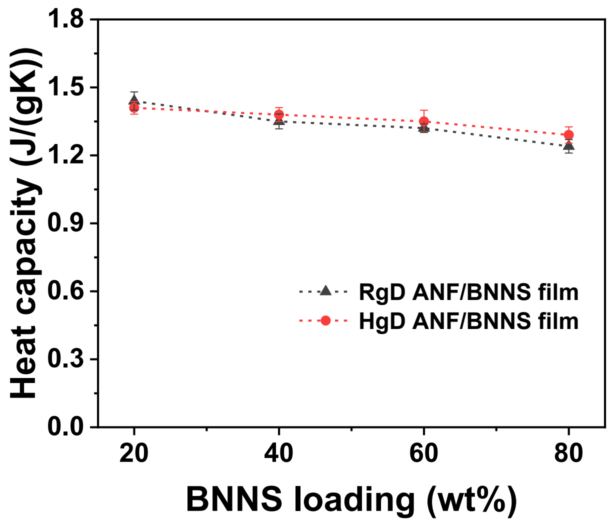

Supplementary Fig. 2. Heat capacity measurements determined by DSC as a function of BNNS loading. Error bars represent standard deviations.

Measurement for Thermal diffusivity α

Thermal diffusivity *α* was measured using a laser flash apparatus (LFA467, NETZSCH). In accordance with the dimensions of the sample tray for the LFA 467 NanoFlash system, the sample to be tested was first cut into a circular disc with a diameter of **25.4 mm** using standard cutter. Subsequently, the thickness (*d*) of samples were measured using caliper (Supplementary Fig. 3). Graphite was coated on the sample surface to minimize surface reflection and enhance laser energy absorption. At a constant temperature of 25 °C, a laser source emitted a pulse of light instantaneously and uniformly irradiated on the lower surface of the sample. The surface layer absorbed the light energy, causing an instantaneous temperature increase, which acted as the hot end to transfer energy to the cold end via one-dimensional heat conduction. An infrared detector is used to continuously measure the corresponding temperature rise in the center of the upper surface, and the temperature rise versus time curve is obtained (**Supplementary Fig. 4**). Thermal diffusivity values are measured at 3 points on the same specimen. The thermal diffusivity α can be calculated according to the equation

$$\alpha = \frac{0.1388d^2}{t_{50}} \tag{S6}$$

where d is the sample thickness and t_{50} is the characteristic time for the sample to heat up to the half of the maximum temperature. The thermal diffusivity values for different samples were calculated using this equation, as illustrated in Supplementary Fig. 5.

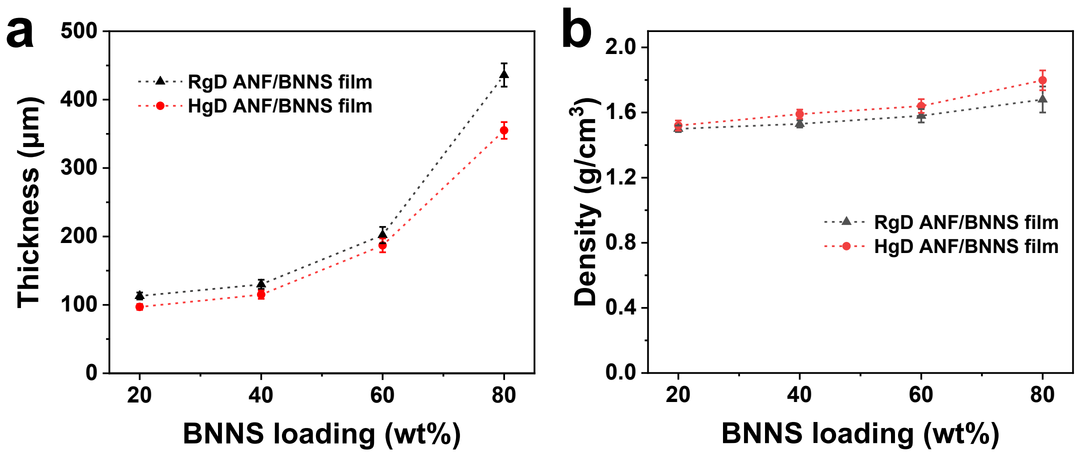

Supplementary Fig. 3. (a) Thickness measurements determined by caliper as a function of BNNS loading. (b) Density ρ of ANF/BNNS film with different BNNS loading. Error bars represent standard deviations.

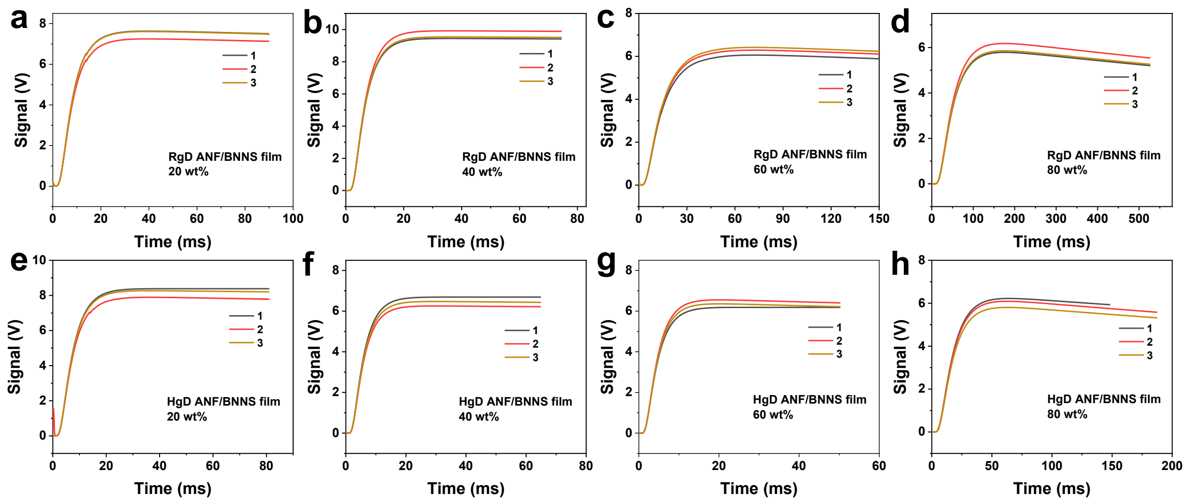

Supplementary Fig. 4. The curves of the temperature (detector signal) increase over time obtained by the laser flash apparatus.

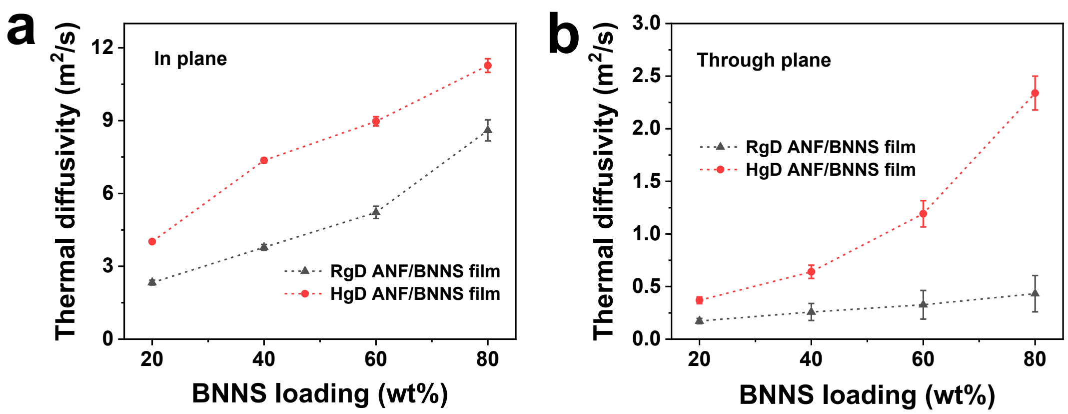

Supplementary Fig. 5. Thermal diffusivity measured with a laser flash method (LFA467). Error bars represent standard deviations.

Measurement for density ρ

Density (ρ) was calculated based on the ratio of weight and volume measurements. The sample to be tested was first cut into a circular disc with a diameter of 25.4 mm using standard cutter. The thickness (d) and weight of samples were measured using caliper and precision electronic balance, respectively. And the results were shown in Supplementary Fig. 3b.

Theoretical calculation formula of cooling power:

The daytime cooling power of cooling HgD ANF/BNNS film can be calculated by:

$$P_{cooling} = P_{rad}(T) - P_{atm}(T_{amb}) - P_{sun} - P_{non-rad} \quad \text{(S7)}$$

where T is the surface temperature of the film, T_{amb} is the ambient temperature; P_{rad} (T) is the thermal radiation power emitted by the film, and P_{atm} (T_{amb}) is the atmospheric thermal radiation power absorbed by the film when the ambient temperature is T_{amb}. P_{sun} is the solar power absorbed by the film, while $P_{non\text{-}rad}$ is the thermal power loss (non-radiative thermal power) due to convection and conduction. In Formula (1), the thermal radiation power P_{rad} (T) emitted by the film is expressed as:

$$P_{rad}(T) = 2\pi \int_0^{\frac{\pi}{2}} d\theta sin\theta cos\theta \int_{2.5\mu m}^{25\mu m} I_{BB}(T,\lambda)\,\varepsilon(\lambda,\theta)d\lambda \quad \text{(S8)}$$

$$I_{BB}(T,\lambda) = \frac{2hc^2}{\lambda^5}\frac{1}{e^{hc/\lambda K_B T}-1} \quad \text{(S9)}$$

In Formula (1), the atmospheric thermal radiation power, P_{atm} (T_{amb}), absorbed by the film is expressed as:

$$P_{atm}(T_{amb}) = 2\pi \int_0^{\frac{\pi}{2}} d\theta sin\theta cos\theta \int_{2.5\mu m}^{25\mu m} I_{BB}(T,\lambda)\,\varepsilon(\lambda,\theta)\varepsilon_{atm}(\lambda,\theta)d\lambda \quad \text{(S10)}$$

Where, ε_{atm} (λ,θ) is the emissivity related to the atmospheric angle and can be expressed as

$$\varepsilon_{atm}(\lambda,\theta) = 1 - \tau(\lambda)^{\frac{1}{cos\theta}} \quad \text{(S11)}$$

Where, τ (λ) is the transmittance of the atmosphere in the zenith direction. P_{sun} refers to the solar power absorbed by the film, which can be expressed as:

$$P_{sun} = \int_{0.3\mu m}^{2.5\mu m} I_{solar}(\lambda)\varepsilon(\lambda,\theta)d\lambda \quad \text{(S12)}$$

Non-radiative thermal power $P_{non\text{-}rad}$ can be expressed as:

$$P_{non-rad} = h_c(T_{amb} - T) \quad \text{(S13)}$$

Where h_c is the coefficient of the non-radiative heat.

We assume an ambient temperature (T_{amb}) of 298 K and four non-radiative heat transfer coefficients (h_c) of 0, 3, 6, and 9 $W/m^2 \cdot K$ to simulate the non-radiative power obtained by thermal conduction and convection between the surface of the radiative cooler and the ambient environment.

Supplementary Note 2.

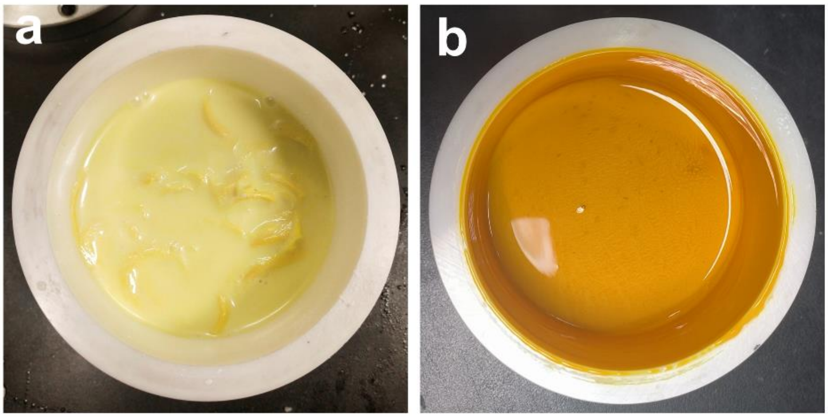

Supplementary Fig. 6. Digital photograph of ANF/BNNS suspension (a) before and (b) after ball milling.

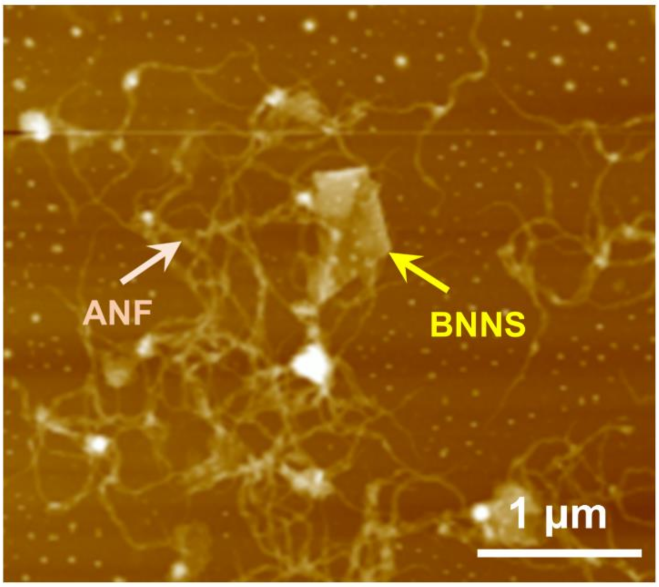

Supplementary Fig. 7. AFM image of ANF/BNNS suspension.

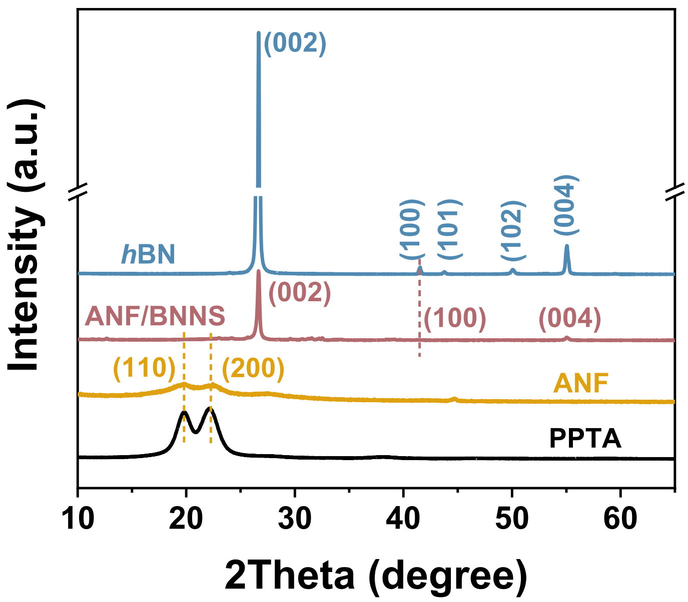

Supplementary Fig. 8. XRD patterns of PPTA, ANF, hBN and ANF/BNNS.

Compared to PPTA fibers, the (110) and (200) diffraction peaks of ANF and ANF/BNNS at 19.8° and 22.1°, respectively, exhibit a weakened intensity, indicating dissociation of the main crystal structure during deprotonation. Simultaneously, in comparison with hBN, the diffraction intensity of BNNS in ANF/BNNS shows a significant decrease for the (002) and (100) peaks along with an evident increase in full width at half maximum (FWHM), suggesting that ball milling-induced mechanical shearing has resulted in the delamination of *h*BN into BNNS.

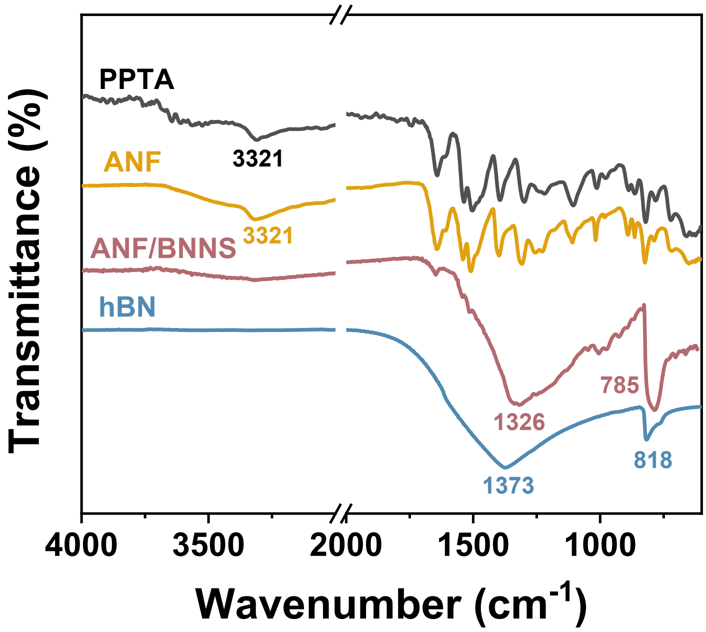

Supplementary Fig. 9. FTIR spectra of PPTA, ANF, hBN and ANF/BNNS.

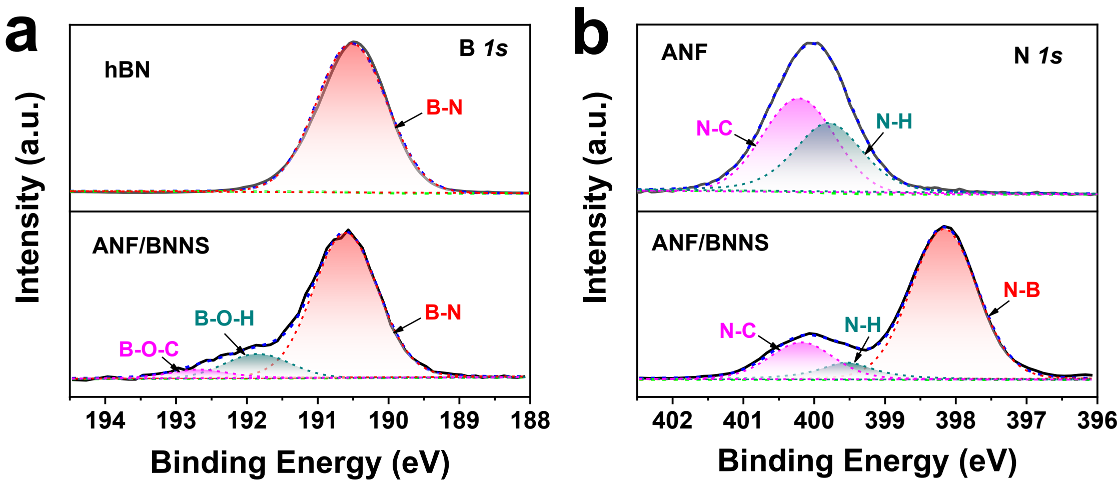

Supplementary Fig. 10. High-resolution XPS analysis of (a) B *1s* and (b) N *1s*.

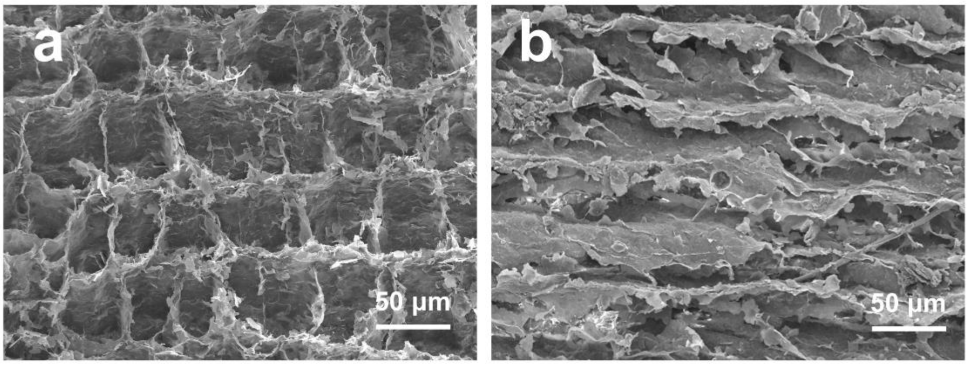

Supplementary Fig. 11. High resolution SEM images of (b) top-view and (c) side-view for honeycomb-like hydrogel skeleton.

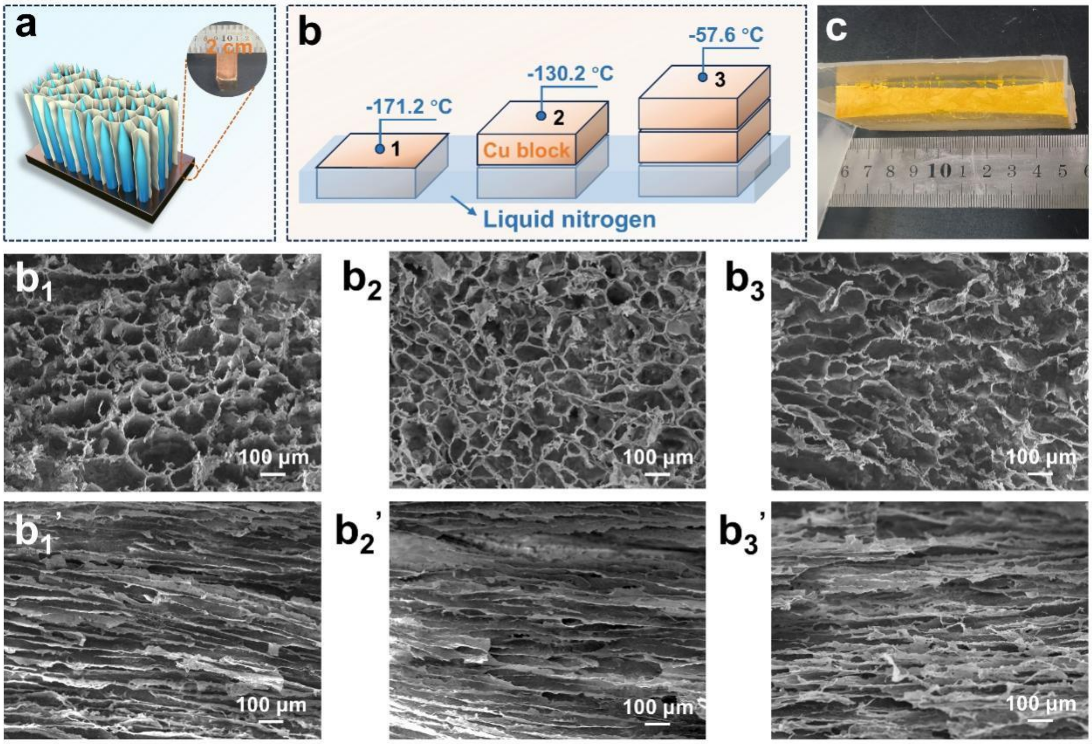

Supplementary Fig. 12. The influence of freezing rate on the construction of honeycomb skeleton. (a) Schematic diagram of directional freezing. (b) Temperature distribution at different heights from the liquid nitrogen plane. (c) Digital image of the ANF/BNNS frozen block. (b_1-b_3) Top and (b_1'-b_3') side view SEM images of ANF/BNNS skeleton under different freezing rates.

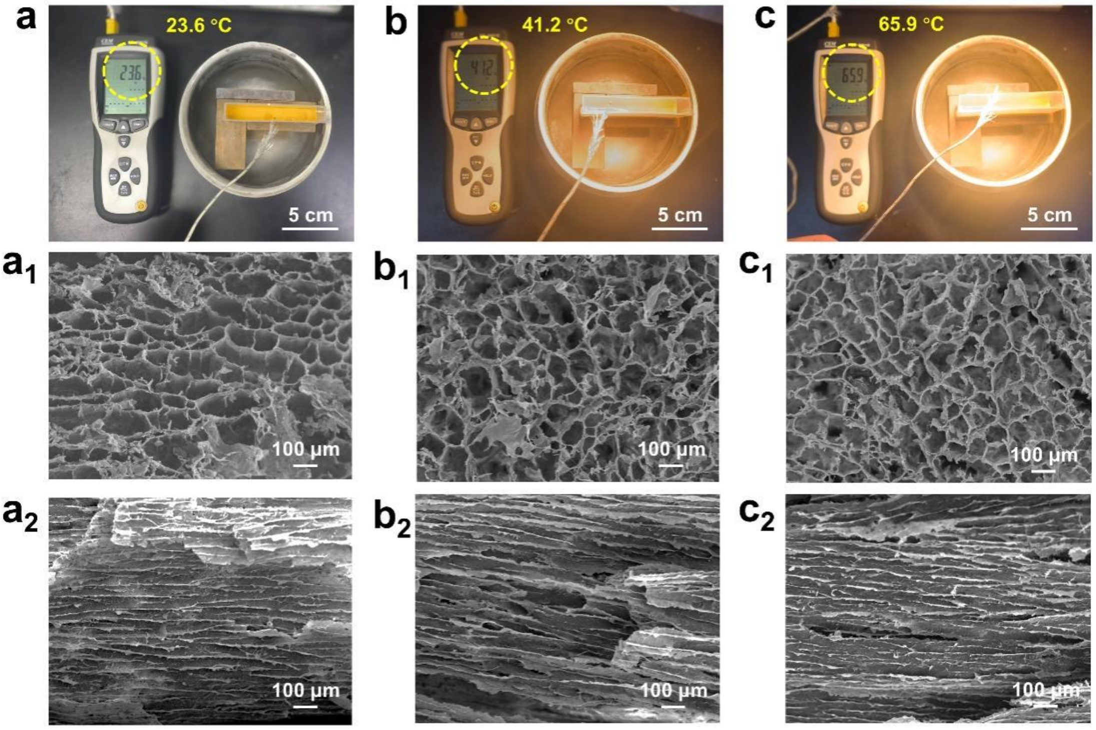

Supplementary Fig. 13. The influence of environmental temperature on the construction of honeycomb skeleton. (a-c) Digital images of the freezing process under various environmental temperature conditions. (a_1-c_1) Top and (a_2-c_2) side view SEM images of ANF/BNNS skeleton under the corresponding environmental temperature conditions.

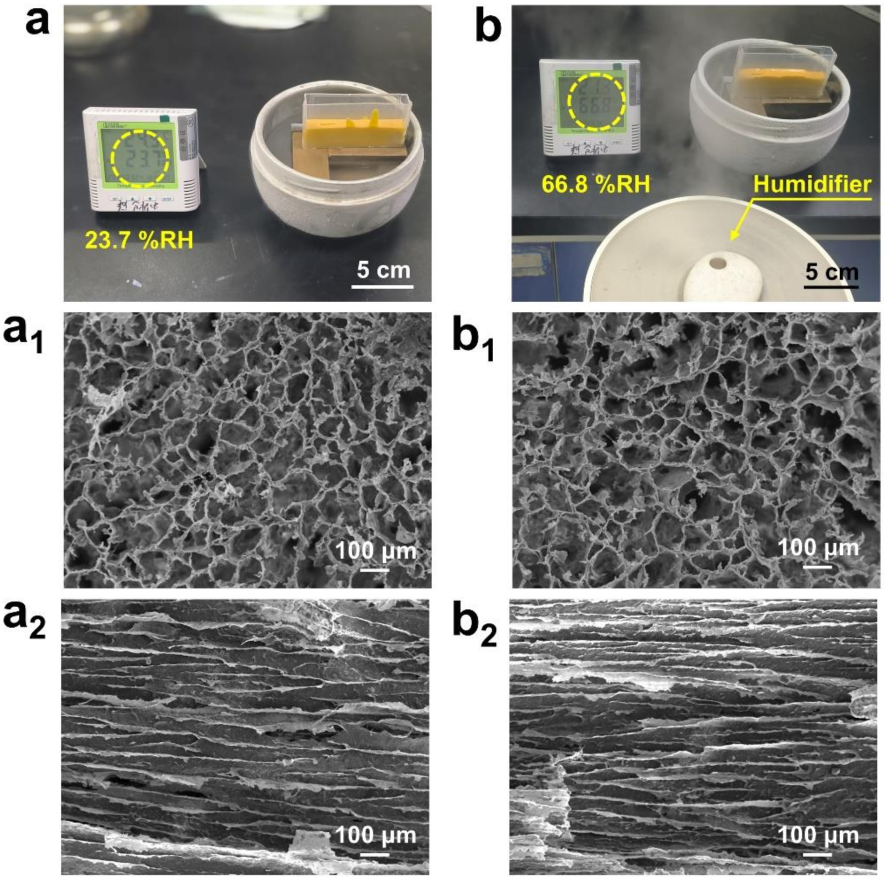

Supplementary Fig. 14. The influence of environmental humidity on the construction of honeycomb skeleton. (a, b) Digital images of the freezing process under various environmental humidity conditions. (a_1, b_1) Top and (a_2, b_2) side view SEM images of ANF/BNNS skeleton under the corresponding environmental humidity conditions.

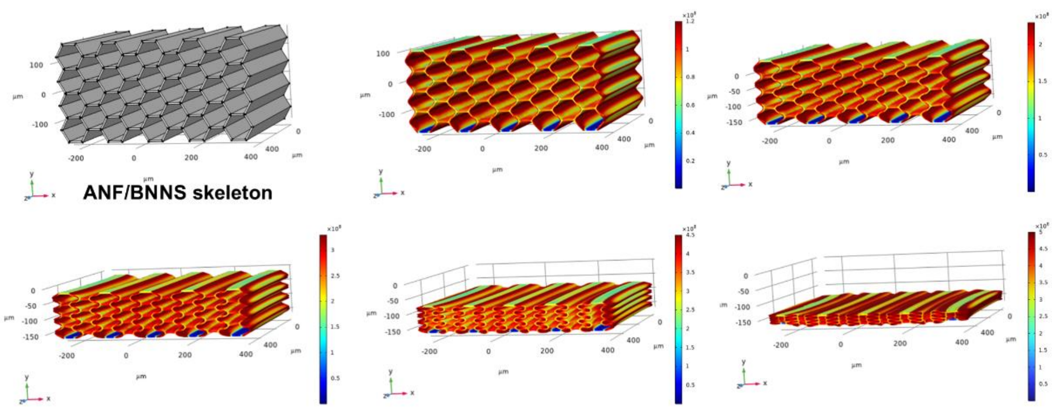

Supplementary Fig. 15. Finite element simulation of stress distribution during the densification process of ANF/BNNS skeleton.

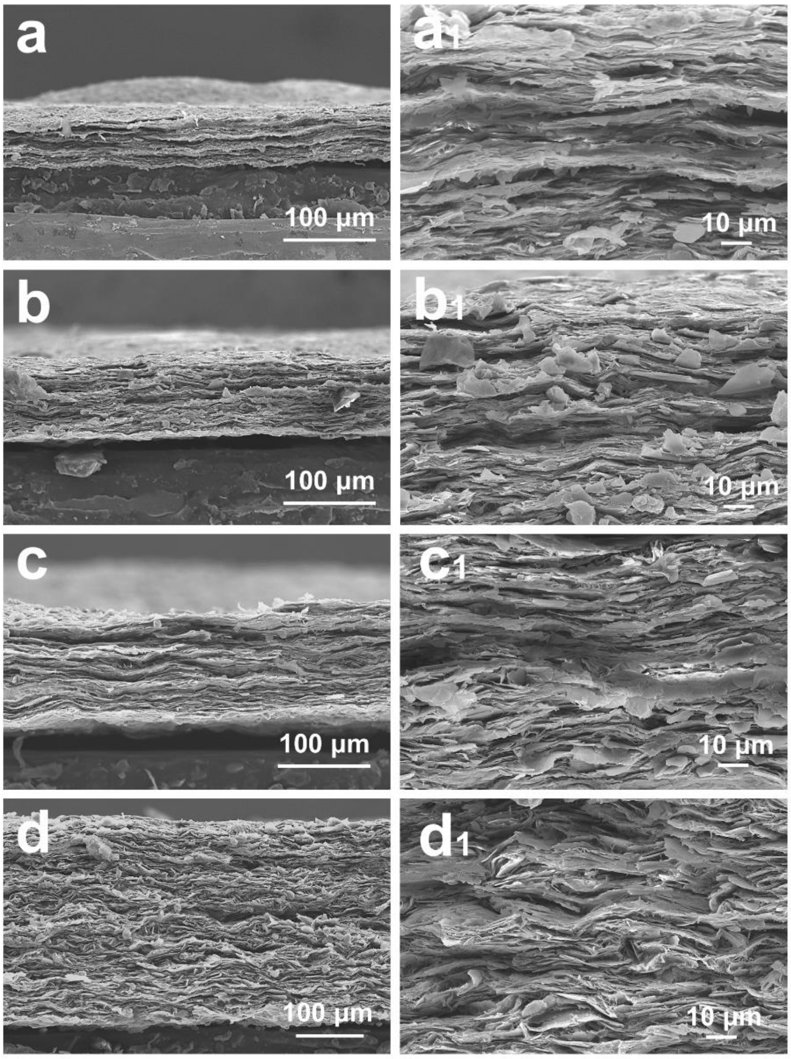

Supplementary Fig. 16. SEM images of top-view for HgD ANF/BNNS film with different BNNS loading.

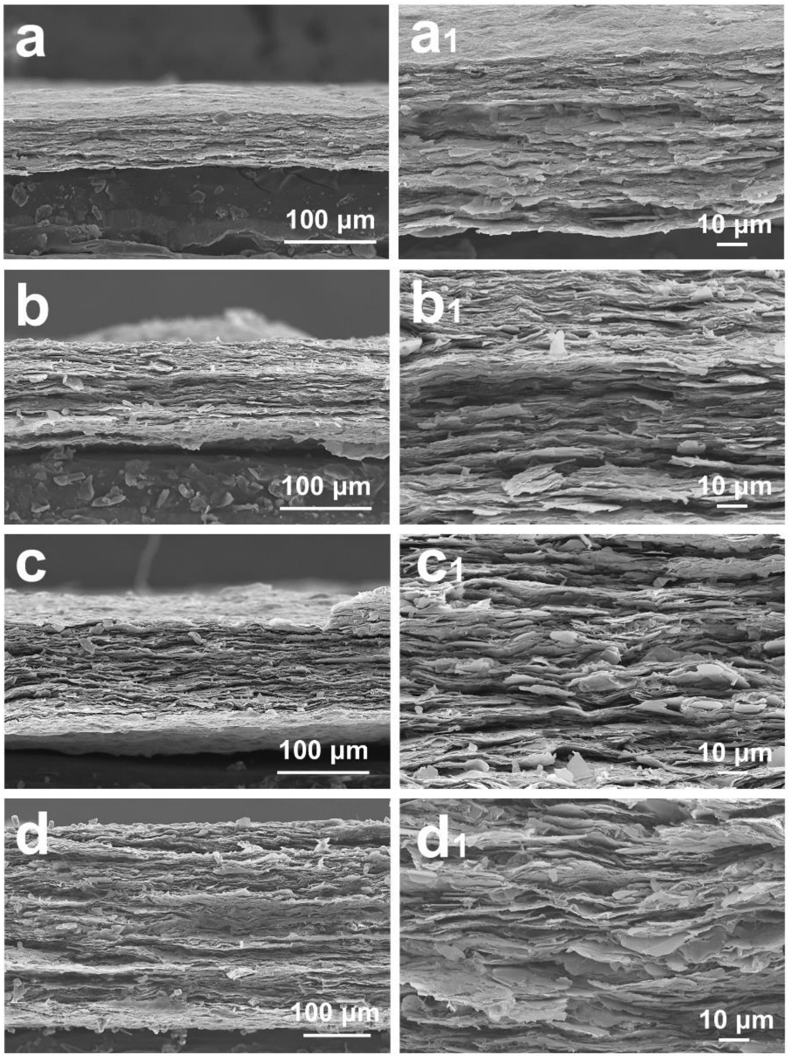

Supplementary Fig. 17. SEM images of side-view for HgD ANF/BNNS film with different BNNS loading.

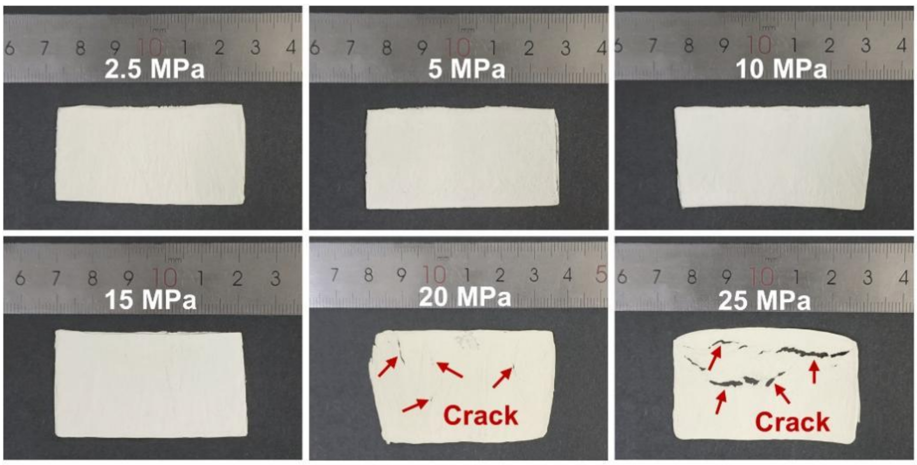

Supplementary Fig. 18. The final film morphology obtained under varying pressures during the densification process.

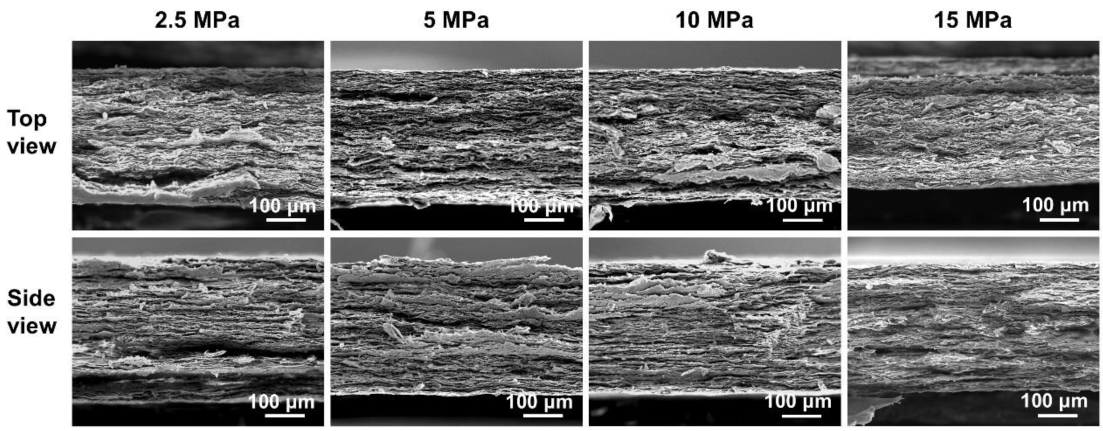

Supplementary Fig. 19. SEM images of top and side views for HgD ANF/BNNS films under various pressures.

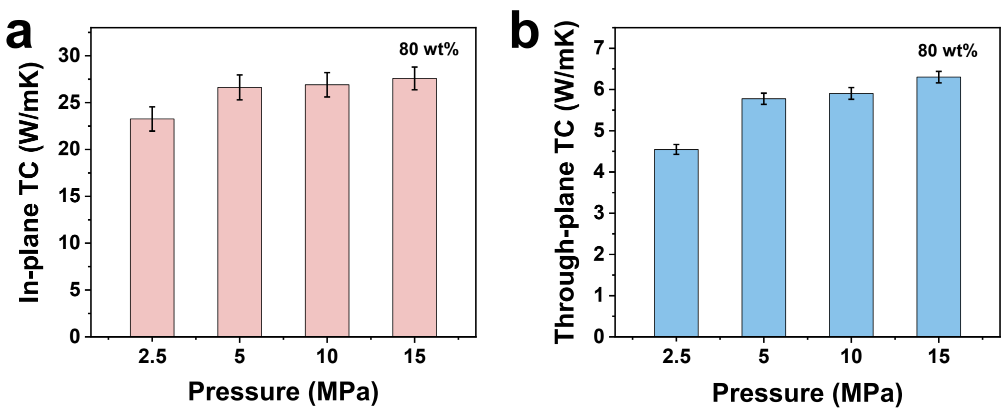

Supplementary Fig. 20. The (a) in-plane and (b) through-plane thermal conductivities of HgD ANF/BNNS films of different pressure. Error bars represent standard deviations.

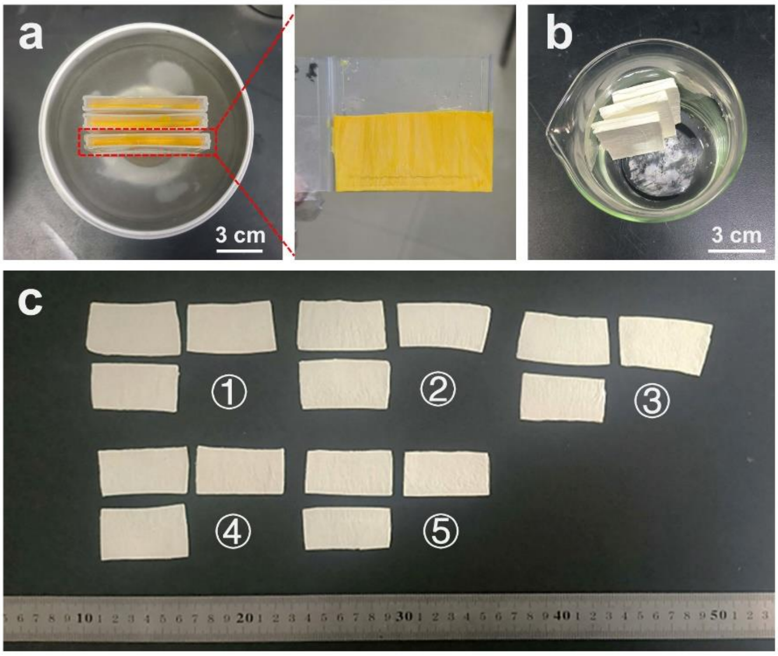

Supplementary Fig. 21. The preparation of HgD ANF/BNNS films involve (a) freeze-casting and (b) thawing-gelation process. (c) Digital images of five batches of HgD ANF/BNNS films.

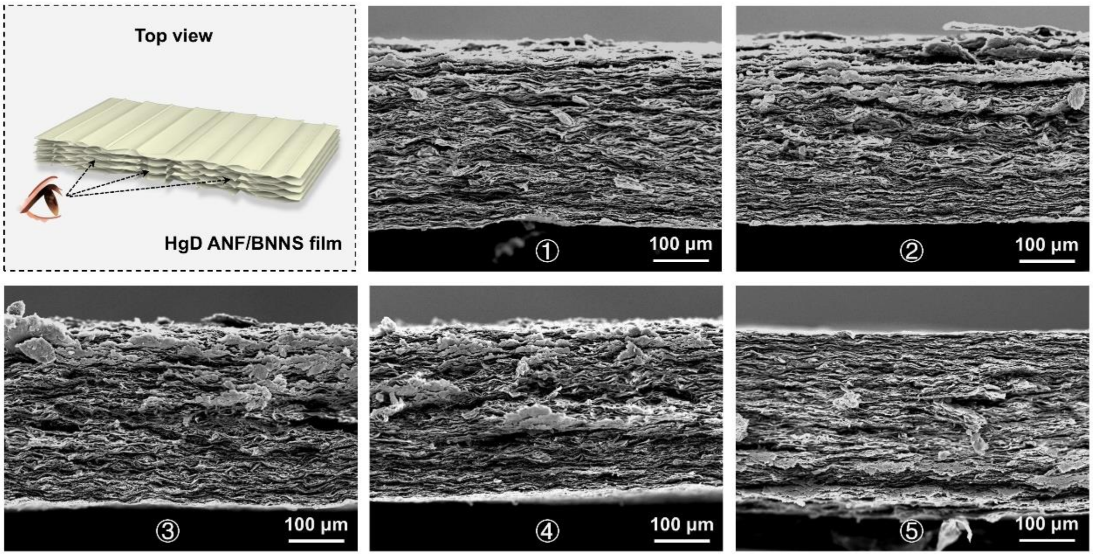

Supplementary Fig. 22. Schematic diagram for the cross-sectional structure of HgD ANF/BNNS film and its cross-sectional morphology.

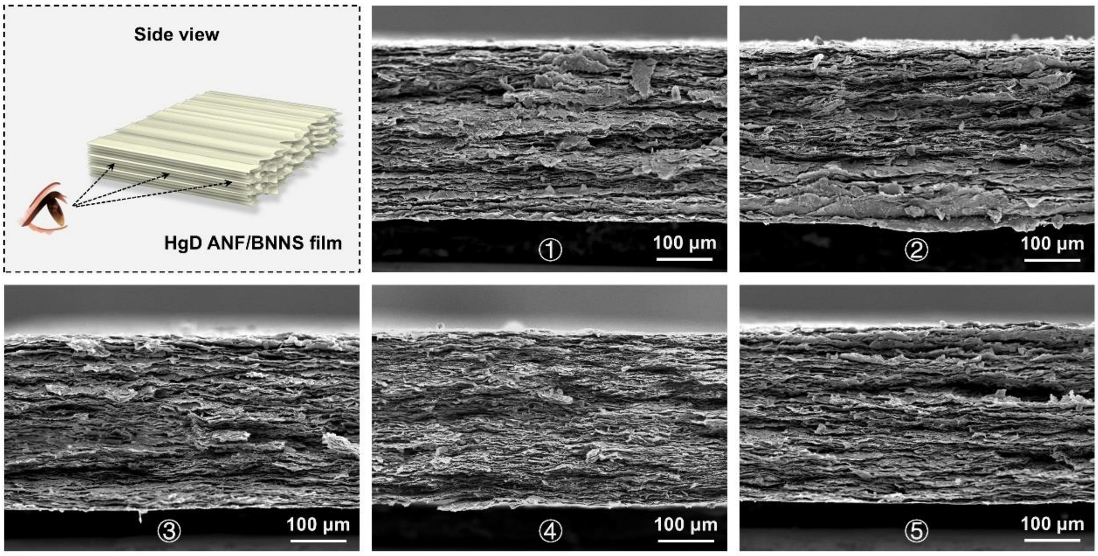

Supplementary Fig. 23. Schematic diagram for the longitudinal structure of HgD ANF/BNNS film and (b') its longitudinal morphology.

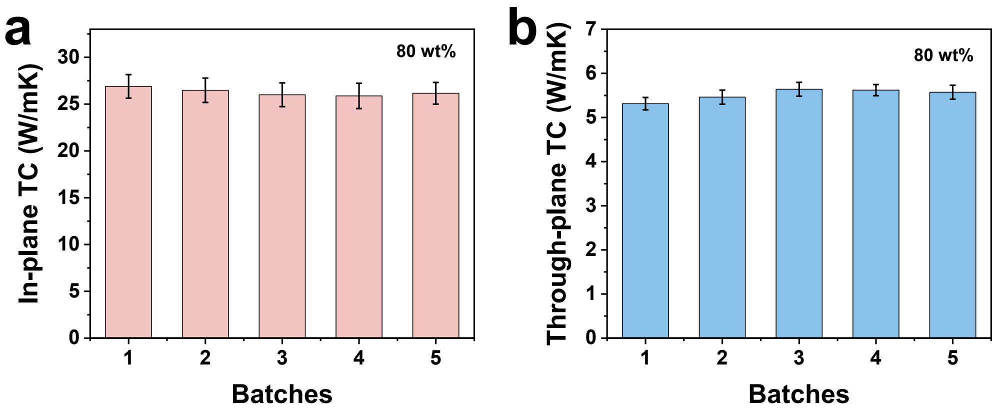

Supplementary Fig. 24. The (a) in-plane and (b) through-plane thermal conductivities of HgD ANF/BNNS films of different batches. Error bars represent standard deviations.

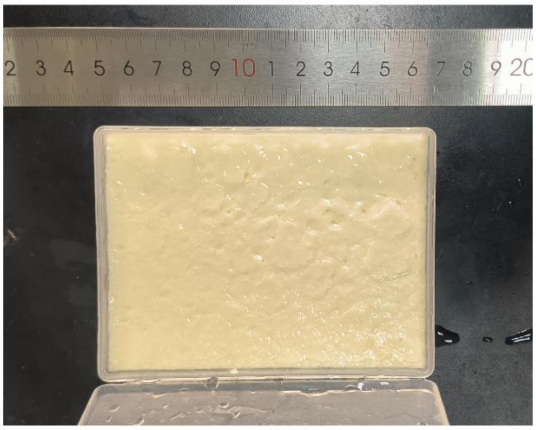

Supplementary Fig. 25. ANF/BNNS gel block after sol-gel conversion.

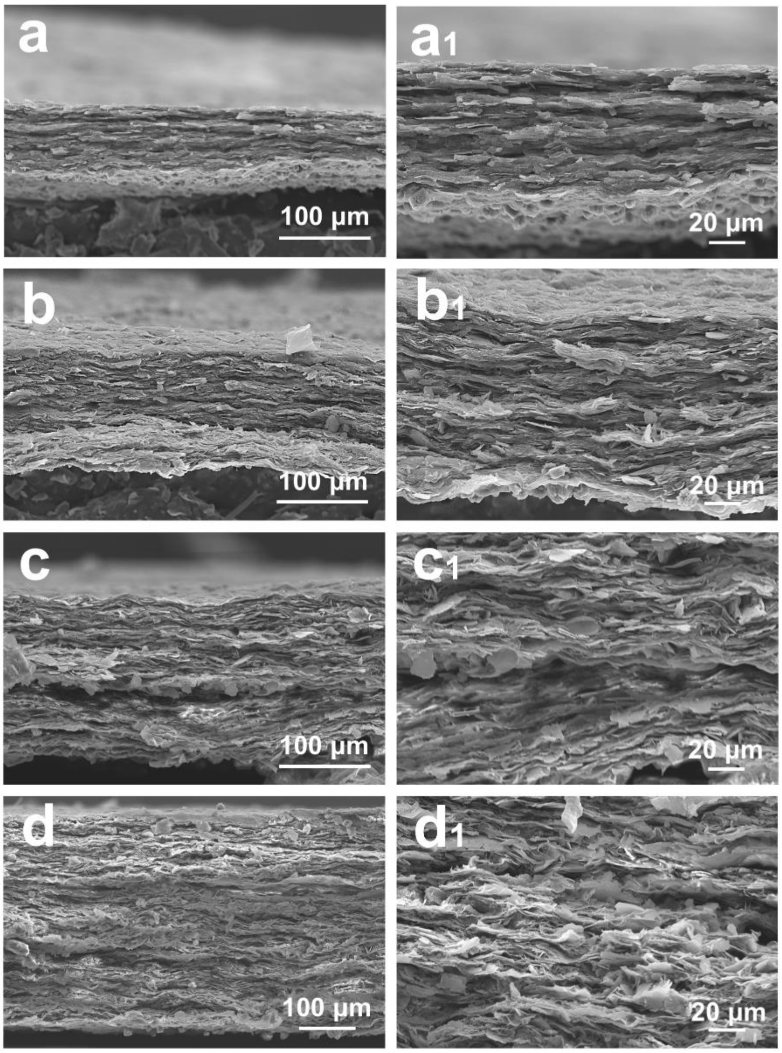

Supplementary Fig. 26. SEM images of RgD ANF/BNNS film with different BNNS loading.

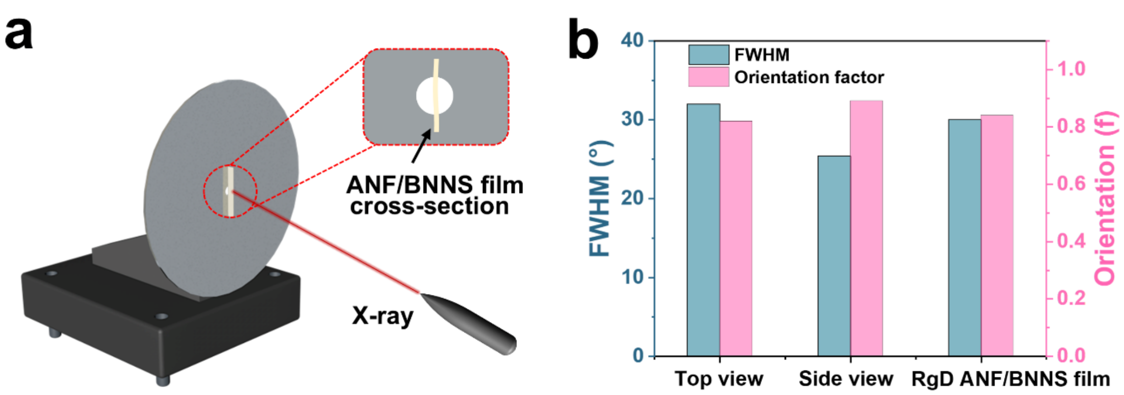

Supplementary Fig. 27. (a) Schematic diagram of the cross-section of ANF/BNNS film irradiated vertically by X-ray. (b) The FWHM and orientation of HgD ANF/BNNS film in different directions and RgD ANF/BNNS film.

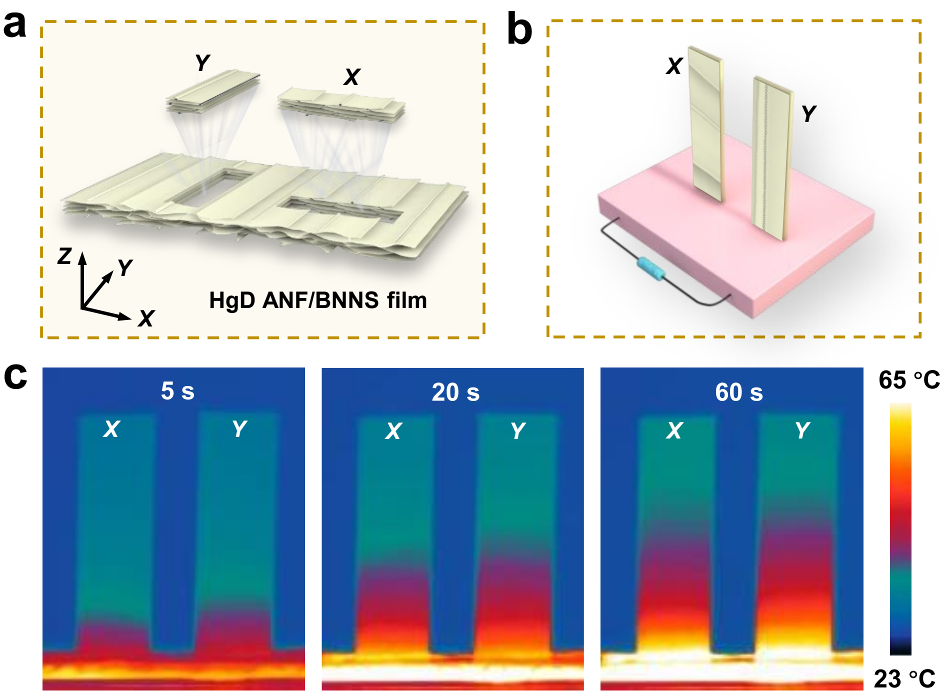

Supplementary Fig. 28. (a) Schematic illustration of the sampling process for HgD ANF/BNNS films along the X and Y-direction. (b) Schematic of heat transfer demonstration set-up and (c) corresponding infrared thermal image.

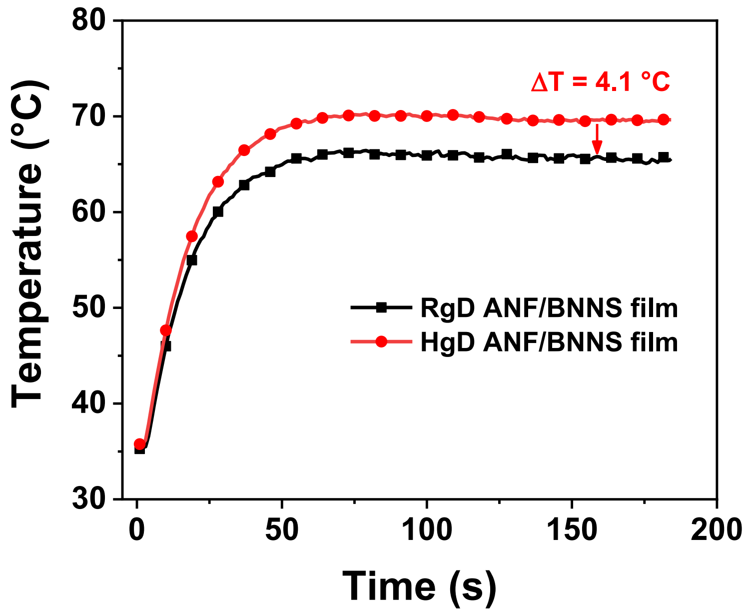

Supplementary Fig. 29. The surface temperature evolution of ANF/BNNS film placed flat on a hot stage.

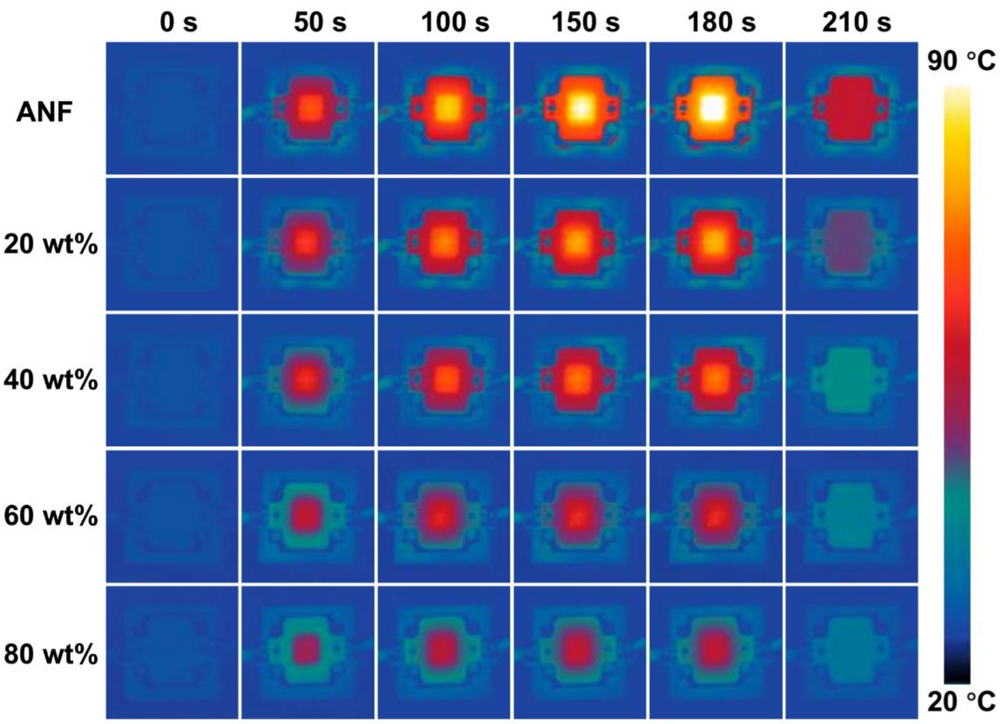

Supplementary Fig. 30. Infrared thermal images for LED chip with HgD ANF/BNNS films as thermal interface materials.

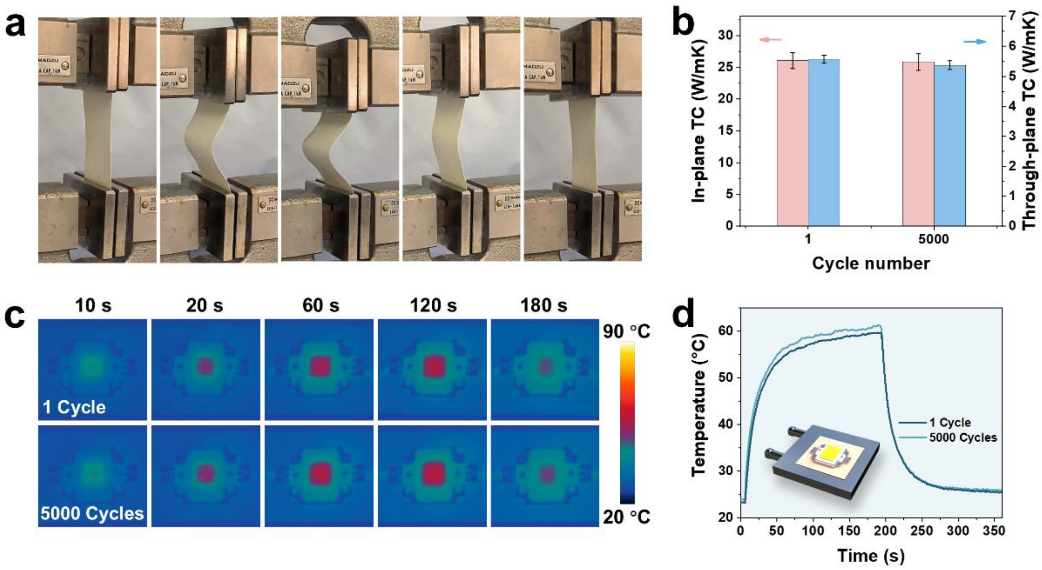

Supplementary Fig. 31. (a) Photographs of the bending cycle process for HgD ANF/BNNS film. (b) Thermal conductivity of 5000 bending cycles of HgD ANF/BNNS film. Error bars represent standard deviations. (c) Infrared thermal images and (d) surface temperature profiles of HgD ANF/BNNS films as TIM between the LED chip and cooling water heat sink for heat dissipation application.

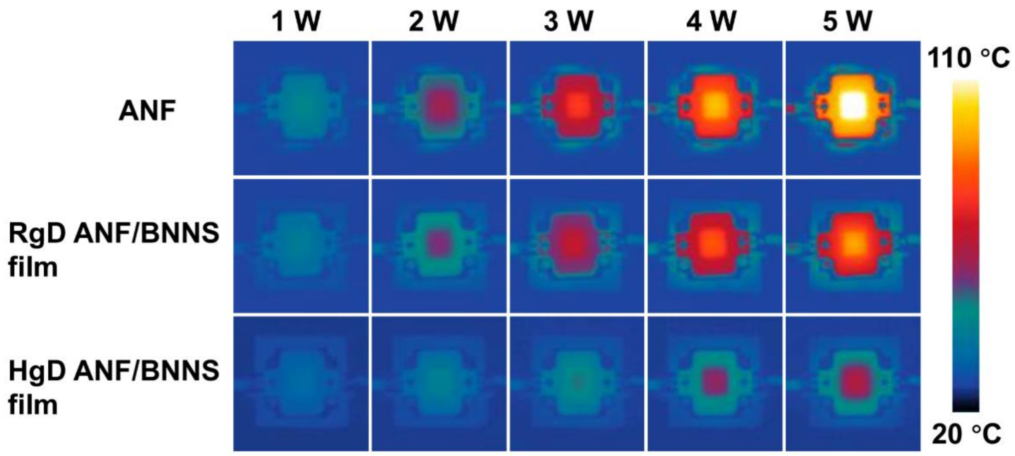

Supplementary Fig. 32. Infrared thermal images for LED chip with ANF, RgD and HgD ANF/BNNS films as TIMs under different powers.

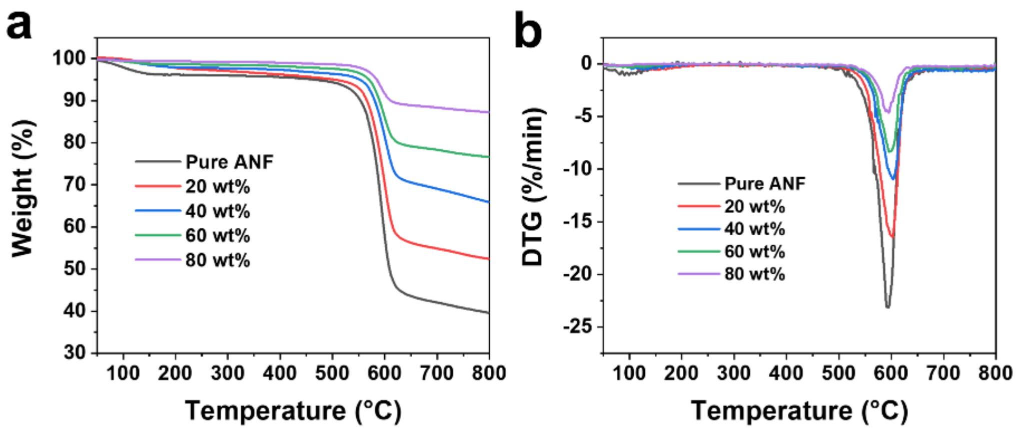

Supplementary Fig. 33. (a) TGA and (b) DTG curves of pure ANF and HgD ANF/BNNS films with different BNNS loadings.

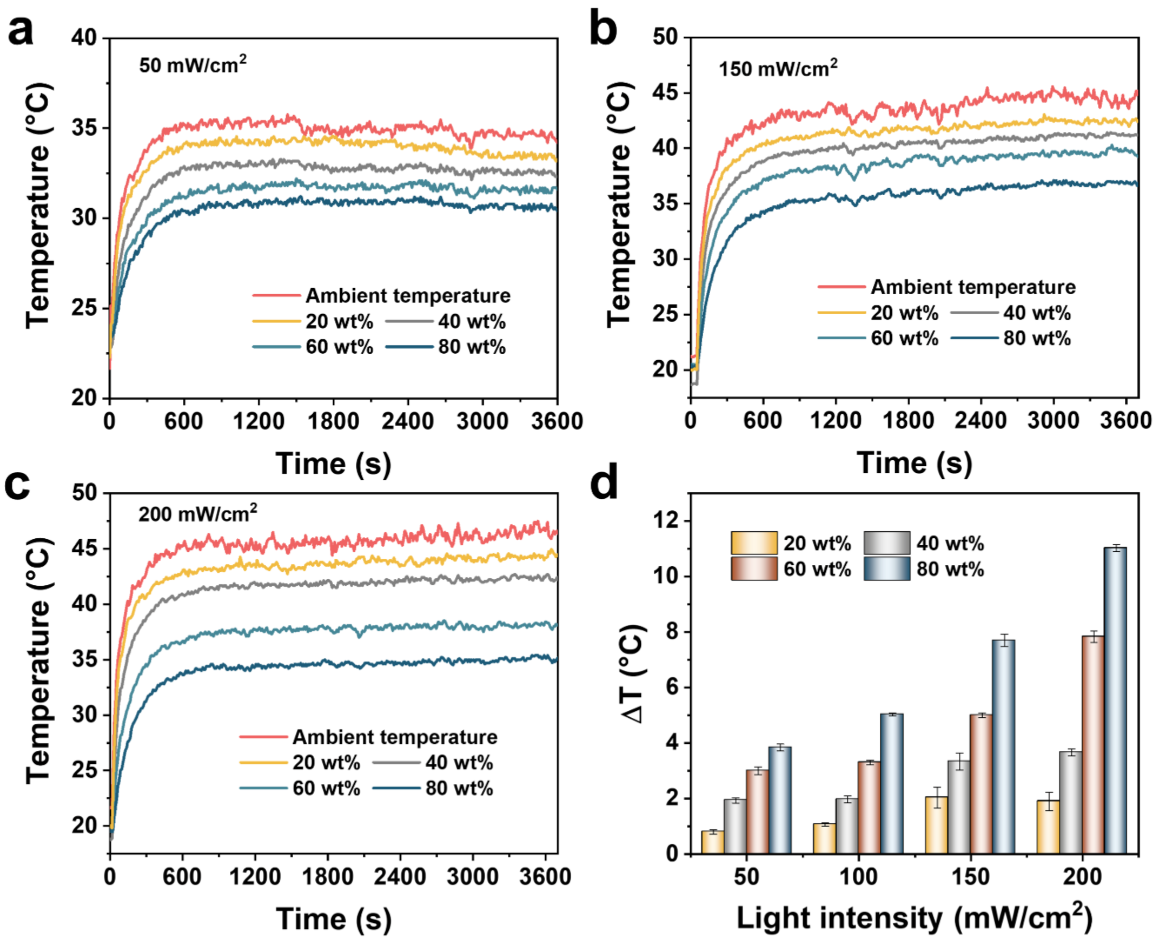

Supplementary Fig. 34. (a-c) Temperature profiles of HgD ANF/BNNS films under different radiation intensity and (d) statistical analysis of the corresponding temperature differences. Error bars represent standard deviations.

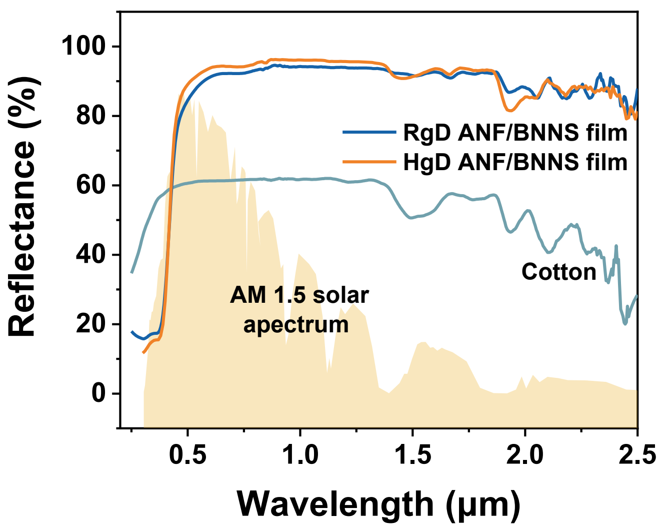

Supplementary Fig. 35. Spectral solar reflection of cotton, RgD ANF/BNNS, HgD ANF/BNNS films.

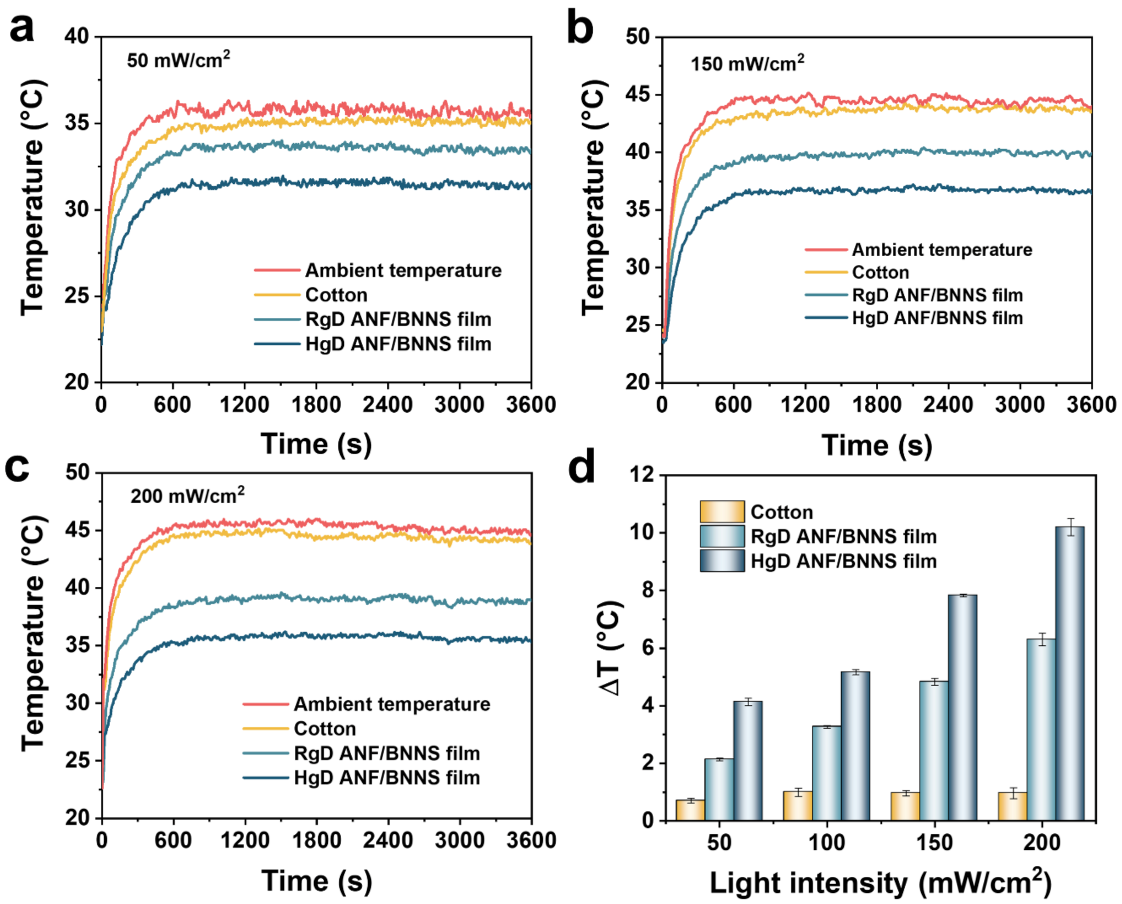

Supplementary Fig. 36. (a-c) Temperature profiles of ambient air, cotton, RgD and HgD ANF/BNNS films under different radiation intensity and (d) statistical analysis of the corresponding temperature differences. Error bars represent standard deviations.

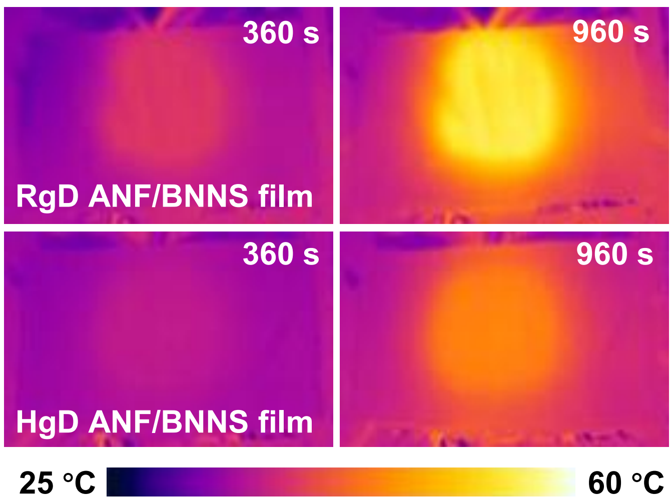

Supplementary Fig. 37. Infrared thermal images (point 2) of ANF/BNNS film.

Supplementary Table 1. Thermal diffusivity (α), Density (ρ), specific heat capacity (C_p) and thermal conductivity (TC) of the films.

Sample		In-plane α (mm^2/s)	Through-plane α (mm^2/s)	ρ (g/cm^3)	C_p (J/gK)	In-plane TC (W/mK)	Through-plane TC (W/mK)
RgD film	20 wt%	2.33	0.172	1.51	1.44	5.03	0.371
	40 wt%	3.78	0.258	1.53	1.35	7.82	0.533
	60 wt%	5.22	0.327	1.58	1.32	10.88	0.683
	80 wt%	8.61	0.432	1.68	1.24	17.57	0.899
HgD film	20 wt%	4.02	0.369	1.52	1.41	8.61	0.79
	40 wt%	7.36	0.641	1.59	1.38	16.16	1.405
	60 wt%	8.97	1.189	1.64	1.35	19.88	2.634
	80 wt%	11.27	2.339	1.79	1.29	26.16	5.425

Supplementary Table 2. Thermal conductivity of HgD ANF/BNNS film in this work and reported literature.

Materials	Fabrication method	Filler Content (wt%)	In-plane TC (W/mK)	Through-plane TC (W/mK)	Year Ref.
EP/BNNS@IL	Blade-casting	45	8.3	0.8	2022[1]
BN/Glass	Coating	100	14	0.4	2018[2]
BNNS-Ag/PVA	Vacuum-assisted filtration	95	13.8	1.09	2016[3]
M-BNNS/PU	Hot-pressing	50	23.8	1.46	2023[4]
SNFs/BNNSs	Vacuum filtration	59.3	3.84	~0.3	2024[5]
f-BN/POSS/PI	In-situ polymerization under pressure	40	17.76	0.75	2024[6]
PVDF/BNNS	Electrospinning and mold pressing	33	10.4	0.49	2019[7]
PS/BNNS	Compressing	13.4 (vol%)	8.0	~0.29	2017[8]
CNFs/BNNS	Vacuum-assisted filtration	50	15.69	0.44	2022[9]
BNNS/PAN	Electrospinning–electrospraying	40	24.98	~0.3	2022[10]
APTES-BNNS/BC	Sol-gel-film conversion	50	24	0.45	2024[11]
HgD ANF/BNNS film	**Honeycomb-gel densification**	**60**	**19.88**	**2.63**	**This work**
		80	**26.14**	**5.43**	

Supplementary Reference

1. Han G*, et al.* Flexible, thermostable and flame-resistant epoxy-based thermally conductive layered films with aligned ionic liquid-wrapped boron nitride nanosheets via cyclic layer-by-layer blade-casting. *Chem. Eng. J.* **437**, 135482 (2022).
2. Wang Y*, et al.* High temperature thermal management with boron nitride nanosheets. *Nanoscale* **10**, 167-173 (2018).
3. Yao Y, Zeng X, Sun R, Xu J-B, Wong C-P. Highly thermally conductive composite papers prepared based on the thought of bioinspired engineering. *ACS Appl. Mater. Interfaces* **8**, 15645-15653 (2016).
4. Yang L, Huang R, Yuan J, Zhang P, Deng J, Li Q. High thermal conductive polyurethane composite films with a three-dimensional boron nitride network in-situ constructed by multi-folding and multi-laminating. *Compos. Sci. Technol.* **245**, 110326 (2024).
5. Wang Y*, et al.* Natural deep eutectic solvent-assisted construction of silk nanofibrils/boron nitride nanosheets membranes with enhanced heat-dissipating efficiency. *Adv. Sci.* **11**, 2403724 (2024).
6. Peng Z, Guo Q, Zhang L, Li C. High thermal conductivity and low dielectric polyimide nanocomposites using diamine-assisted mechanochemical exfoliation boron nitride and in-situ polymerization under pressure. *Chem. Eng. J.* **488**, 150824 (2024).
7. Chen J, Huang X, Sun B, Jiang P. Highly thermally conductive yet electrically insulating polymer/boron nitride nanosheets nanocomposite films for improved thermal management capability. *ACS Nano* **13**, 337-345 (2019).
8. Wang X, Wu P. Preparation of highly thermally conductive polymer composite at low

filler content via a self-assembly process between polystyrene microspheres and boron nitride nanosheets. *ACS Appl. Mater. Interfaces* **9**, 19934-19944 (2017).

9. Hu D, Liu H, Yang M, Guo Y, Ma W. Construction of boron nitride nanosheets-based nanohybrids by electrostatic self-assembly for highly thermally conductive composites. *Adv. Compos. Hybrid Mater.* **5**, 3201-3211 (2022).

10. Wang H*, et al.* An electrospinning–electrospraying technique for connecting electrospun fibers to enhance the thermal conductivity of boron nitride/polymer composite films. *Compos. Part B: Eng.* **230**, 109505 (2022).

11. Yu B, Luo Z, Zhou Y, Zhang Q, He J, Fan J. Highly thermally conductive flexible biomimetic APTES-BNNS/BC nanocomposite paper by sol–gel-film technology. *ACS Appl.Mater. Interfaces* **16**, 21050-21060 (2024).